



Structural defects in LiMn_2O_4 induced by gamma radiation and its influence on the Jahn-Teller effect



Renier Arabolla Rodríguez^a, Eduardo L. Pérez-Cappe^{a,*}, Yodalgis Mosqueda Laffita^a, Armando Chávez Ardanza^b, Jaime Santoyo Salazar^c, Manuel Ávila Santos^d, Miguel A. Aguilar Frutis^d, Nelcy Della Santina Mohalem^e, Oswaldo Luiz Alves^f

^a Ionic conducting materials Laboratory, Institute of Materials Science and Technology (IMRE) of Havana University, CP 10400 Havana, Cuba

^b Department of Radiology, Center of Applied Technologies and Nuclear Development (CEADEN), CP 10400 Havana, Cuba

^c Instituto Politécnico Nacional, CINVESTAV, CP 07360 Ciudad de México, Mexico

^d Instituto Politécnico Nacional, Centro de Investigación en Ciencia Aplicada y Tecnología Avanzada (CICATA), Legaria 694, Del. Miguel Hidalgo, C.P. 11500 Ciudad de México, Mexico

^e Universidade Federal de Minas Gerais, Departamento de Química, Laboratório de Materiais Nanoestruturados, Belo Horizonte, Minas Gerais 31270-901, Brazil

^f Solid State Chemistry Laboratory, Institute of Chemistry, Campinas University, P.O.Box 6154, 13083-970 Campinas, SP, Brazil

ARTICLE INFO

Keywords:

LiMn_2O_4

Jahn-Teller effect

Structural defects

ABSTRACT

The influence of Jahn-Teller (JT) distortion on the electrochemical behavior of LiMn_2O_4 is not fully understood nowadays. This paper concerns the role that structural defects play in reducing the magnitude of JT distortion. Structural defects were induced in micrometric and nanometric LiMn_2O_4 using ^{60}Co gamma radiation. Techniques such as X-ray diffraction (XRD), high-resolution transmission electron microscopy (HRTEM), and magic angle spinning spectroscopy (^7Li MAS NMR) were used to detect and investigate the defects created by ^{60}Co gamma irradiation in micrometric and nanometric LiMn_2O_4 . Differential scanning calorimetry (DSC) was used to study the effect on the JT distortion enthalpy. Spectroscopic and microstructural modifications of LiMn_2O_4 produced by the action of radiation are shown for the first time. The results revealed that partial and total edge dislocations are generated after the oxides are irradiated. In the formed dislocations, manganese and lithium ions modified their surroundings and coordination, while the atomic positions of oxygen atoms changed in the fcc structure. These modifications gave rise to a decrease in the magnitude of JT distortion in the micrometric oxides, while no distortion was detected in the nanometric oxides. Because of the defects in LiMn_2O_4 caused by ^{60}Co gamma irradiation, a minor distortion in the cell parameter (c/a) should be expected when this material is used as a cathode in lithium-ion batteries.

1. Introduction

The storage of large quantities of energy in a reversible, safe and inexpensive manner is a necessity for the technological and societal development of mankind. Among the frequently studied cathodic materials for lithium secondary batteries, LiMn_2O_4 appears to be a promising candidate because of its low cost, low toxicity and compatibility with the environment [1, 2]. However, the moderate stability and low theoretical energy density (592 Wh/Kg) of the LiMn_2O_4 with respect to other competitive cathode materials as LiCoO_2 (1037 Wh/Kg) and LiFePO_4 (612 Wh/Kg) are weaknesses that need to be overcome for its application.

The theoretical energy density of LiMn_2O_4 is reached when the lithium composition (x) in the general formula $\text{Li}_x\text{Mn}_2\text{O}_4$ is between 0

and 1 (4 V zone). Unlike LiCoO_2 and LiFePO_4 , the structure of LiMn_2O_4 allows it to exceed $x = 1$ and reach a value of $x = 2$ (3 V zone), where the stored density energy would theoretically be 1042 Wh/kg. This places this material in an advantageous position compared with its competitors.

Transitioning from $x = 1$ to $x = 2$ remains a great challenge that requires much research [2–5], due to the presence of Jahn-Teller (JT) distortion [2]. This effect is responsible for the irreversible structural transition from the cubic to the tetrahedral phase. The JT effect considerably affects the reversibility of the insertion/deinsertion processes and creates high cell polarization even at low cycling current [1]. In addition, the JT effect produces strain between particles during the anisotropic transport of Li^+ inside the material [2, 3].

Attempts have been made to reduce the JT effect; however,

* Corresponding author.

E-mail address: cappe@imre.uh.cu (E.L. Pérez-Cappe).

<https://doi.org/10.1016/j.ssi.2018.06.007>

Received 29 November 2017; Received in revised form 4 June 2018; Accepted 5 June 2018
Available online 19 June 2018

0167-2738/ © 2018 Elsevier B.V. All rights reserved.

strategies involving doping with elements such as Mg^{2+} , Fe^{3+} , Co^{2+} , Ni^{3+} , Al^{3+} , and Li^+ only achieved a stabilized structure, thus enhancing the number of charge-discharge cycles or increasing the average working voltage up to $\sim 5\text{ V}$ [6, 7]. In highly Ni-doped spinel ($\text{LiMn}_{1.5}\text{Ni}_{0.5}\text{O}_4$), it is possible to overcome JT distortion and as a consequence improve the specific capacity to $\sim 160\text{ mA}\cdot\text{h/g}$ [8].

In this context, the best strategy to reversibly cycle over the 4 V and 3 V zones is to use nanoparticles of LiMn_2O_4 [1, 2, 9, 10]. In that respect M. Okubo et al. [1] demonstrated that very good results can be obtained by using nanoparticles with sizes $< 15\text{ nm}$, because of the interphase between the cubic and tetragonal structures, which makes lithium-ion transport difficult, does not take place. This results because the small size of the nanocrystals avoids the long-range cooperative interaction responsible for decreasing the driving forces that give rise to this transition [1].

In addition the work of Y.J. Park et al. [3] showed that low crystalline films of LiMn_2O_4 with defects such as micropores, microvoids and vacancies considerably improve the reversible insertion of Li^+ in all the composition range ($0 < x < 2$) [3, 5].

Bearing in mind the relation between the JT effect and reversibility in the insertion/deinsertion process, it is unusual that only a few papers can be found in the literature arguing the influence of particle size or defects on the JT distortion of LiMn_2O_4 . The majority of these works relate the morphology or microstructural characteristics of these materials with the enhancement of the reversibility of the cycling process. In this way, the possible influence that structural and microstructural defects could have over the magnitude of the JT distortion is often obviated. Experimentally, it is possible to create a variety of structural and microstructural defects in lithium and manganese oxides by employing ^{60}Co gamma radiation, which would help us understand the influence of such defects on JT distortion [14, 15]. However, only a few works have examined the effect of gamma radiation on LiMn_2O_4 [16]. The greatest efforts from the theoretical and experimental points of view have been addressed on the MgAl_2O_4 spinel type structure. Nevertheless, we can infer what will happen to LiMn_2O_4 upon irradiation, as these two oxides are isostructural and the ionic radius of Mg^{2+} (0.58 \AA) and Li^+ (0.59 \AA), as well as Al^{3+} (0.53 \AA) and Mn^{4+} (0.53 \AA), are quite similar.

Several theoretical articles support the idea that the main point defects caused by irradiation in MgAl_2O_4 could be related to the exchange of the positions of Mg^{2+} and Al^{3+} (cation anti-site defect) [11, 12] and although this fact is difficult to detect, some indirect results have been reported [13, 14]. Experimentally, a great amount of microstructural transformations in this oxide, such as dislocation loop punching, creation of amorphous tracks with typical diameters of a few nm, and atomic disordering, have been observed [15].

Therefore, the aim of this work is to show that structural, microstructural modifications, such as ionic shifts and dislocations, respectively, directly influence the magnitude of the JT distortion in LiMn_2O_4 , and that these aspects are very important to consider when a larger energy storage range is desired.

In this work, we address defective LiMn_2O_4 obtained by ^{60}Co gamma irradiation of its micrometric and nanometric particles.

This work consists of two main sections. The first section describes the most important defects generated as a consequence of ^{60}Co gamma irradiation of this oxide.

The second part of the work discusses how defects can influence JT distortion with the corresponding reduction in the magnitude of the JT enthalpy and how this could be related to the cubic-tetragonal structural transition.

2. Experimental

2.1. Synthesis and irradiation

The micrometric LiMn_2O_4 was synthesized from a citrate precursor

of manganese III and Lithium with a molar relation Li: Mn: Citrate 1:2:3 as was reported in [16]. This citrate precursor was placed in a platinum crucible and decomposed at $750\text{ }^\circ\text{C}$, in air, during 30 min.

A portion of the resulted micrometric oxide was separated and irradiated with ^{60}Co gamma rays in an irradiator model ISO-GAMMA LL-CO at an irradiation rate of 4.874 kGy/h by periods of 12 h until a cumulative dose of 630 kGy was reached.

Nanometric oxide was obtained from the same citrate precursor for the micrometric sample described above, but its thermal decomposition was carried out at a heating rate of $10\text{ }^\circ\text{C/min}$ at $350\text{ }^\circ\text{C}$ over 40 min in air flux [16].

The as-prepared nanoparticles were irradiated at 100, 630, and 1000 kGy at the same irradiation rate as used for micrometric oxide.

2.2. Characterization

X-ray diffraction patterns of the as-prepared irradiated and non-irradiated oxides were obtained with a Shimadzu XRD700 XRD diffractometer by using a Cu target submitted to 30 mA electronic radiation at a voltage of 40 kV. Measurements were carried out in a 2θ range of $17\text{--}70^\circ$ at a scan speed of $0.025^\circ/\text{s}$ and a counting time of 4 s. A standard crystalline Si (CAS #: 7440-21-3, No ICSD: 27-1402) sample was used for instrument calibration. Cell parameter refinement was done according to the Le Bail method [17] with the aid of the FullProf [18] program.

The data used to perform structural analysis by the Rietveld method were recorded with a Bruker D8 Advance diffractometer using a Ge (111) Johansson monochromator and an X-ray wavelength of 1.5406 \AA at room temperature. Overall, 2208 experimental points were acquired over the 2θ range.

^7Li -RMN (MAS) spectra were obtained using Bruker 400 MHz equipment. $^7\text{LiCl}$ (116.57 MHz) was used as a reference material to calibrate the chemical shifts. Measurements were performed using a holder with a diameter of 4 mm at a temperature of $25\text{ }^\circ\text{C}$. Magic angle gathering over 500 scans in every register with a radiofrequency pulse of $\pi/2$, width of $2.4\text{ }\mu\text{s}$ and relaxation time of 1 s was employed. Different rotation frequencies (10 and 13 KHz) were used to determine the position of the isotropic peak.

The oxides were studied by transmission electron microscopy (TEM) using a JEOLJEM-2010 microscope with a LaB_6 filament operating at 200 kV. The point-to-point resolution was 0.21 nm for high-resolution transmission electron microscopy (HRTEM). The samples were supported on carbon copper grids, and digital images were acquired using a CCD camera and digital micrograph software from GATAN.

Differential Scanning Calorimetry (DSC) was used for the quantitative determination of the influence of irradiation on the (ΔH_{JT}) magnitude of the JT effect of these oxides at low temperature. DSC measurements were carried out using DSC Q10 V9.4 equipment. Cyclic heating and freezing processes were performed in a nitrogen atmosphere between 20 and $-90\text{ }^\circ\text{C}$ at a heating rate of $\pm 5\text{ }^\circ\text{C/min}$. Aluminum pans and aluminum oxide were used as holders and the reference material, respectively. The instrumental precision and accuracy for the enthalpy change were 2% and 7%, respectively, when employing Hg(l) as the reference material. UV-Vis measurements were performed on the micrometric and nanometric samples by using a Spectrophotometer UV-Vis Hitachi U 2010. The samples were dispersed in water using an ultrasound bath during 15 min. The experiments were done between 200 and 1000 nm with a scan speed of 3 nm/s and a path length of 1 nm.

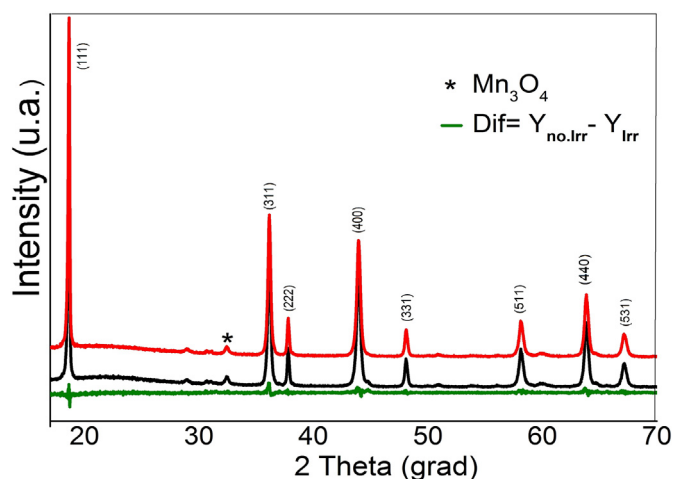


Fig. 1. XRD measurement of the micrometric LiMn_2O_4 oxides: Non-irradiated oxide (black line), irradiated oxide (red line), difference pattern (green line). (For interpretation of the references to color in this figure, the reader is referred to the web version of this article.)

3. Results

3.1. Characterization of the effect of gamma ^{60}Co radiation on micro and nano- LiMn_2O_4

3.1.1. Micrometric LiMn_2O_4 oxide

The as-prepared micrometric oxide crystallized in a cubic spinel-type structure with a space group $\text{Fd-}3\text{m}$ and cell parameter of $a = 8.240 \text{ \AA}$ (see black line in Fig. 1). The sample exhibits good crystallinity, which is reflected both in the value obtained for the cell parameter and in the peak width. Nevertheless, a small amount of Mn_2O_3 impurity can be observed in the XRD pattern.

After irradiation at 630 kGy, no significant modification in the XRD pattern is detected, as can be observed from the difference diffraction pattern of both oxides (see red line in Fig. 1). This means that defects formed as a consequence of irradiation are present in too small of a concentration to be detected in bulk samples by conventional XRD.

The SEM study showed that the as-prepared micrometric oxide is characterized by a heterogeneous crystallite size (see Fig. 2a). Micrometric and sub-micrometric clusters, such as microspheres, were observed. The electron diffraction pattern of this material (Fig. 2b) was indexed in the [111] direction with an interlayer distance for this plane of 4.75 \AA , which is quite close to that obtained by XRD (4.76 \AA).

The fast Fourier transform (FFT) shows the electron diffraction contribution at several selected areas (Fig. 2c) in the irradiated sample and staking of the atomic plane along the LiMn_2O_4 lattice after irradiation (Fig. 2d). Small changes in the planes orientation can be observed for the [220] and [111] directions (boxes a and b in Fig. 2c, respectively). For the irradiated sample, arrays of edge dislocations are observed in low-angle frontiers, as seen in Fig. 2c and d. In Fig. 2d, a large increase of the interlayer distance is observed in the [111] direction (box a in Fig. 2d) compared with a non-defective area (box b in Fig. 2d). This fact is a measure of the great plane distortion suffered by the cationic polyhedral sites around these defective areas, possibly caused by the displacement of ions after irradiation.

The empty interstitial position 16c and the position 8a occupied by lithium ions in the spinel LiMn_2O_4 structure are located in the space between the (111) planes; thus, these two sites should be affected by the new location of the shifted ions.

The ^7Li NMR-MAS spectra of both materials, irradiated and non-irradiated, offer valuable information about the local surroundings of the ^7Li nuclei (see Fig. 3).

In the deconvoluted spectrum of the non-irradiated sample (Fig. 3a),

a main band centered at 534 ppm is observed, which is attributed to Li^+ ions in the 8a tetrahedral position [19]. One additional small band can be observed at 602 ppm overlapped with the sideband closer to the main signal (Fig. 3a). This small band can be attributed 1) the presence of Li^+ ions in the empty 16c octahedral position (Li_i^+) [20] or 2) lithium ions in their normal spinel sites, but near defects in the lattice [19]. The relative quantity of Li ions presents in one of these two possible positions (1%) was calculated by integrating the area under the peaks.

After the irradiation, an increase in the area of the band centered at 602 ppm and an asymmetric decay of the ^7Li NMR-MAS spectrum can be observed (Fig. 3b and c). These two observations are related to the 10–17% increase in the lithium population in the new chemical surroundings (see Fig. 3c). Shifted Li ions can settle in 16c positions to form the Li_i^+ defect. On the other hand, some of the 8a tetrahedral can be distorted as a result of shifted neighboring atoms. The small nuclear charge and electronic density of Li^+ does not allow it to greatly interact with radiation; thus, the modification of the Li^+ distribution in the material could be interpreted as a consequence of the interaction of the Li^+ ions with heavier ions, such as Mn^{3+} and Mn^{4+} . In addition the modification of the Li^+ distribution can stem from their movement to the vacancy created by Mn ions (creating $\text{Li}_{\text{Mn}}^{2+}$ or $\text{Li}_{\text{Mn}}^{3+}$ defects). The large atomic charge and electronic density of Mn^{3+} and Mn^{4+} ions, makes manganese to be the main target of the radiation and consequently causes these ions to undergo atomic shifts that give rise to the formation of stable defects inside the crystal.

Two possible phenomena can be considered to explain the experimental results obtained above by HRTEM and ^7Li RMN-MAS. First, ^{60}Co irradiation can provoke a shift in the Mn ions to the 16c position, creating Mn_i^{3+} or Mn_i^{4+} defects and their couple $\text{V}_{\text{Mn}}^{2+}$ and $\text{V}_{\text{Mn}}^{3+}$, respectively. The Li^+ tetrahedron located close to these defects are expected to suffer large distortions. The other possibility is the creation of cation anti-site defects ($\text{Mn}_{\text{Li}}^{2+}$ or $\text{Mn}_{\text{Li}}^{3+}$ together $\text{Li}_{\text{Mn}}^{2+}$ or $\text{Li}_{\text{Mn}}^{3+}$, respectively). In these anti-site defects, manganese and lithium ions switch their structural positions giving rise to the formation of a dipolar system as occurs between Mg^{2+} and Al^{3+} in spinel MgAl_2O_4 [11, 12].

Finally, oxygen shifting and oxygen vacancies can be expected as a consequence of irradiation as also occurs in MgAl_2O_4 spinel and MgO oxide [21–23]. When this happens, V centers (two oxygen, one of them ionized, $\text{O}^{2-}-\text{O}_i^-$) are formed and F or F^+ centers (oxygen vacancies V_O^{2+} or V_O , respectively) appear to compensate the charge. These defects directly influence the geometry of the Li^+ tetrahedron and contribute to the 602 ppm signal. An assignment of O defects creation is usually made by observing UV–Vis absorptions about 3.2 (V center) and 5.3 eV (F centers), see the figure of supplementary file. Using this technique, any transition has been observed in the micrometric material because the larger particle size in micrometric particles makes the concentration of defects be small and the overlapping of the defects bands with the huge band of interband transitions $\text{O}(2p)\text{-Mn}(t2g)$ and $\text{O}(2p)\text{-Mn}(eg)$ makes difficult to observe modifications in the spectrums. Nevertheless, these defects cannot be neglected. Proves of this will show out further studying the nanometric material.

Whatever the new positions of the shifted Mn ions, a large distortion will take place as a consequence of interaction with their new surroundings.

The structural defects in general can introduce a different mechanism of stress relaxation [24, 25], playing a special role during cycling of the cathodic material [26] but also have influence over the magnitude of the JT effect.

In Fig. 4, the formation mechanism of the defects because of irradiation is shown, which influences the enthalpy related to the reversible JT distortion, which occurs in this material at approximately 10°C .

As seen in Fig. 4, for the non-irradiated sample, a peak corresponding to JT distortion is observed during cooling. The transition of the non-irradiated sample begins at 11.4°C , and the corresponding phase transition enthalpy during cooling and heating was 4.49 J/g and 2.65 J/g , respectively (see Table 1).

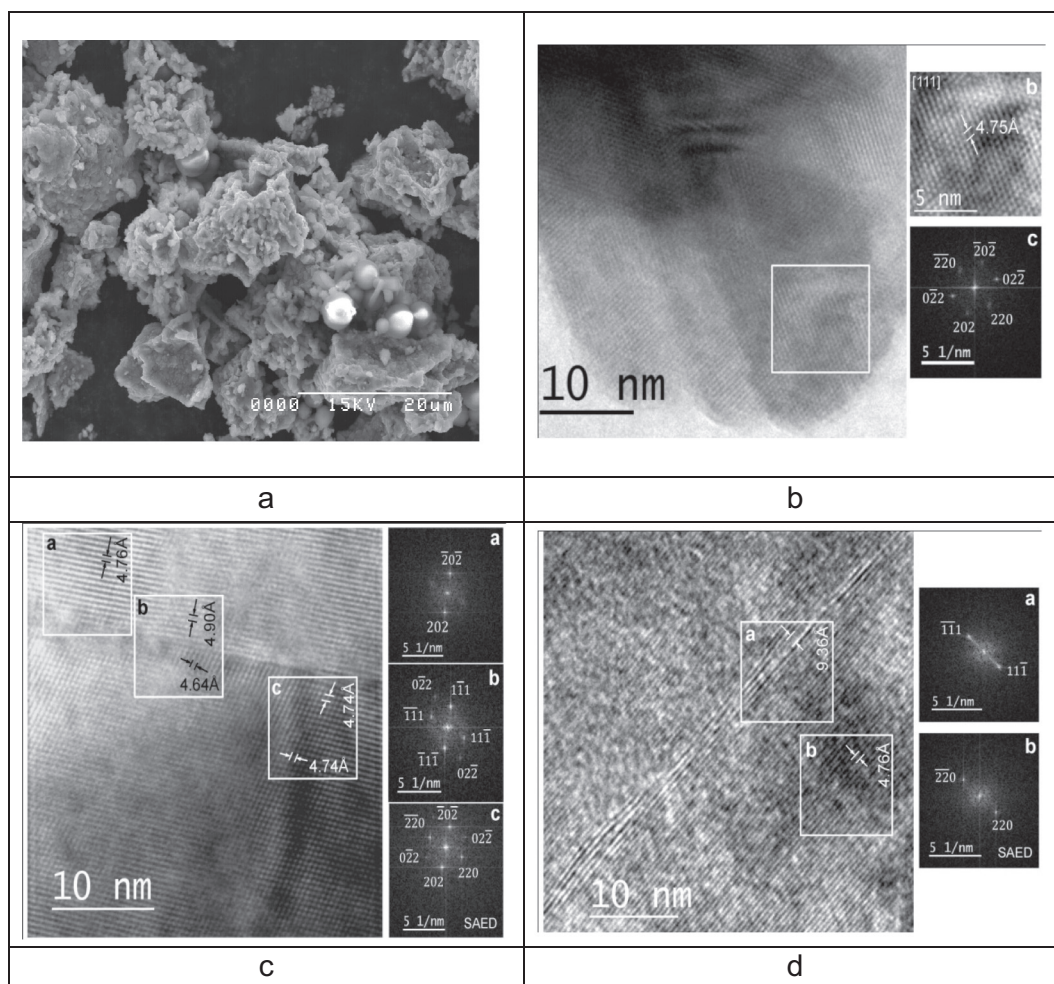


Fig. 2. SEM (a) and HRTEM (b) images of the non-irradiated micrometric LiMn_2O_4 oxide. HRTEM images (c and d) of the LiMn_2O_4 oxide irradiated at a dose of 630 kGy.

The irradiated sample also exhibits a peak corresponding to JT distortion that presents two distinct effects during the first cooling cycle (Fig. 4). The resulting overall enthalpy (see Table 1) is 24 % lower than the corresponding energy of the non-irradiated sample.

Successive heating and cooling cycles of the irradiated oxide, as shown in Fig. 4, converge in a caloric profile similar to that observed for the non-irradiated sample, with the difference that this profile corresponds an enthalpy value 28% lower than that of the non-irradiated oxide.

The caloric profile in the first cycle of the irradiated sample had a different magnitude (Fig. 4), whereby the lower value of the enthalpy associated with JT distortion is unequivocal evidence of the creation of local defect environments in the material. These new environments are related to the new surroundings of some of the Li^+ ions, as was observed by the ^7Li NMR-MAS technique, but this result can also arise from the new manganese octahedral positions responsible for the magnitude of the JT distortion.

The model that we propose to explain the decrease in the magnitude of the JT distortion is discussed in the next section.

3.1.2. Nanometric LiMn_2O_4 oxide

The variation in the lattice parameter (Δa) vs the irradiation dose (i.e., 100, 630 and 1000 kGy) is shown in Fig. 5a. The trend shows very interesting behavior, featuring an increase in the lattice parameter at low doses (≤ 100 kGy) and a decrease at higher doses (≥ 600 kGy). The increase in the lattice parameter with doses has been previously reported in lithium-manganese spinel oxides irradiated with 30 kGy

gamma radiation [27] while its behavior at high doses has not been reported. This behavior is clearly observed in the XRD patterns of irradiated LiMn_2O_4 . First, the diffraction maxima shift to lower angles with an irradiation dose of up to 100 kGy and then back to higher values with an increase in the irradiation dose from 100 to 1000 kGy (Fig. 5b).

Changes in the cell parameter are not observed for the sample with micrometric-sized particles, which reflects the greater capacity of the nanomaterials to display the influence of defects inside the structure with respect to the bulk materials. The observed trend shows the existence of a threshold in the relation between the lattice parameter and dose because of the accumulation and relaxation of defects in the nanometric material.

To establish the influence of stable defects on the structural parameters over a long period of time (2 years), Rietveld analysis was carried out on a non-irradiated sample and the same sample after 2 years of irradiation at 100 kGy (see Tables 2 and 3, respectively).

The non-irradiated oxide presents a lattice parameter $a = 8.205(1)$ Å, Table 2. After 2 years, the same sample irradiated at 100 kGy exhibited a lattice parameter $a = 8.208(2)$ Å (Table 3), which gives a difference between these two values of 0.003 Å. Though the cell parameter was still greater than that of the non-irradiated sample, the magnitude Δa decreased by approximately 6.5 times with respect to a recently irradiated sample. Additionally, a slight distortion in the oxygen position can still be observed (Table 3). The decrease in Δa after 2 years of the irradiation shows that relaxation mechanisms allow the structure to partially return to its initial state.

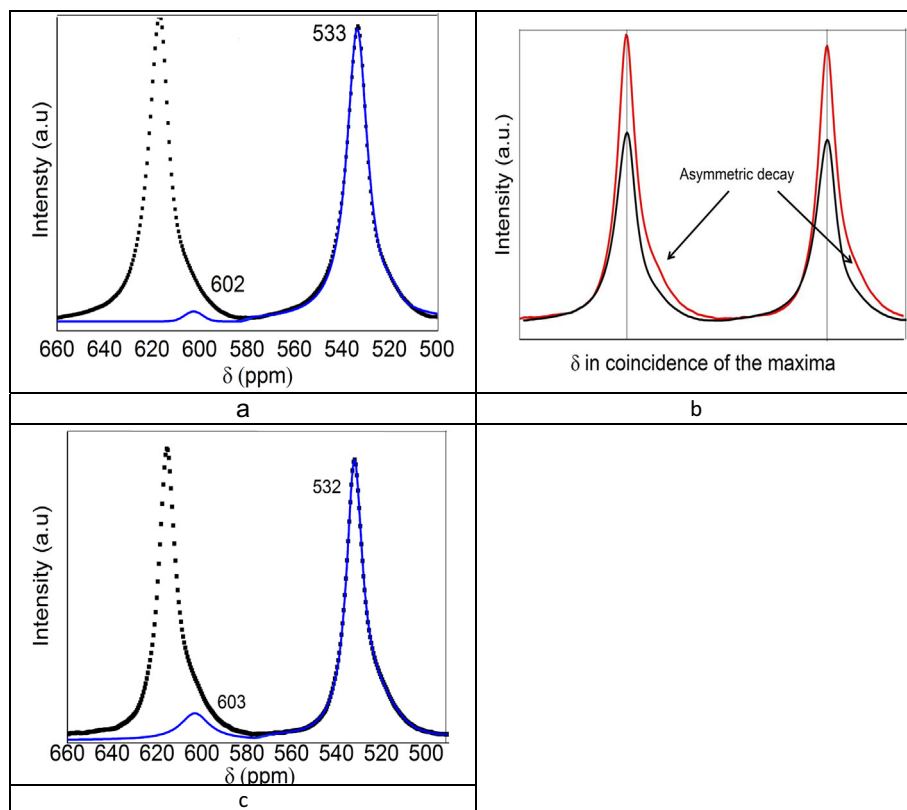


Fig. 3. ^7Li NMR-MAS spectra of the micrometric LiMn_2O_4 oxide: a) non-irradiated oxide, b) superposition of the non-irradiated (line black) and irradiated (line red) oxides spectra and c) irradiated LiMn_2O_4 oxide at 630 kGy. The magic angle spinning speed used was 13 kHz. (For interpretation of the references to color in this figure legend, the reader is referred to the web version of this article.)

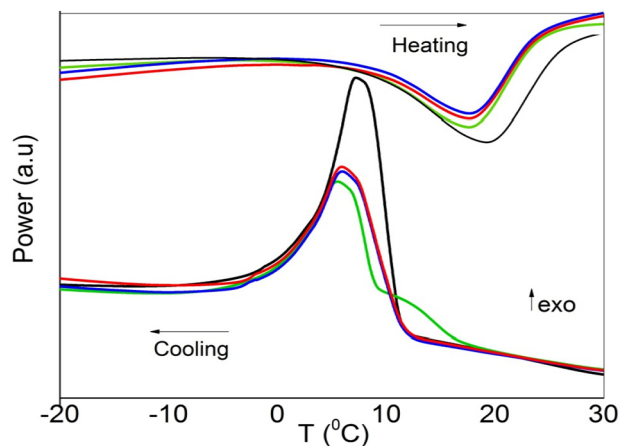


Fig. 4. DSC measurements of micrometric non-irradiated sample (black) and irradiated at 1st cycle (green), 3rd cycle (red) and 4th cycle (blue). (For interpretation of the references to colour in this figure legend, the reader is referred to the web version of this article.)

Table 1

Jahn-Teller enthalpy of the cooling and heating processes for the irradiated and non-irradiated micrometric samples.

Sample	ΔH_{JTcool} (J/g)	ΔH_{JTHeat} (J/g)
Micro-LMO	4.49 ± 0.13	2.65 ± 0.07
Irradiated 1st cycle	3.40 ± 0.10	2.39 ± 0.07
Irradiated 4th cycle	3.24 ± 0.10	2.33 ± 0.07

Because XRD is a bulk technique, only the average characteristics of a structure can be measured. This prevents the possibility of detecting the influence of minor defects, such as microstructural defects, that

have rather large average structural impacts, furthering our understanding of the Δa vs. dose behavior and the decrease in Δa overtime.

Fig. 6 shows the effect of irradiation on the microstructure of nanometric lithium-manganese oxide for doses of 100 kGy and 630 kGy.

As can be observed in Fig. 6a and b, the nanometric oxide irradiated below the threshold has the same morphological characteristics as the non-irradiated sample, while the nanometric oxide irradiated at 630 kGy (Fig. 6d) presents noticeable morphological and microstructural changes with respect to the non-irradiated oxide and the oxide irradiated at 100 kGy.

Studying the microstructure of the irradiated nanometric materials shown in Fig. 6c and e, it can be observed that due to the irradiation, edge dislocation occurs inside the crystallite, similar to the micrometric oxide. In the material irradiated at a low dose, shown in Fig. 6c, it is possible to observe partial and total dislocations. These partial dislocations are produced by the movement of atoms in the fcc structure from their normal position to an intermediate position described by the vector b_1 (Fig. 7). In this new position, a change in the symmetry takes place, which induces large structural strain. Thus, at the beginning of the irradiation process, atomic displacements related to the change in symmetry of the Mn ions in the material occur. The generated strain seems to be responsible for the increase in the cell parameter observed by XRD (Fig. 5b). With an increase in irradiation dose and therefore the number of formed defects, total dislocations and morphological modifications are produced. In a total dislocation, the plane of displaced atoms returns to its initial symmetry configuration through a route marked by the vector b_2 , and a total displacement (b_3) is produced, as shown in Fig. 7. The annihilation of defects on the surface and the restoration of the initial symmetry of the Mn ions in the dislocation eliminate the initially created strain, which enables the cell parameter to recover its initial value, as shown in Fig. 5b.

Similar to the micrometric LiMn_2O_4 sample, in the ^7Li NMR-MAS experiment of the nanometric oxide, the signal corresponding to Li^+ atoms in the 8a positions appears at ~ 534 ppm, without any significant modification by the different doses, as shown in Fig. 8. In these spectra,

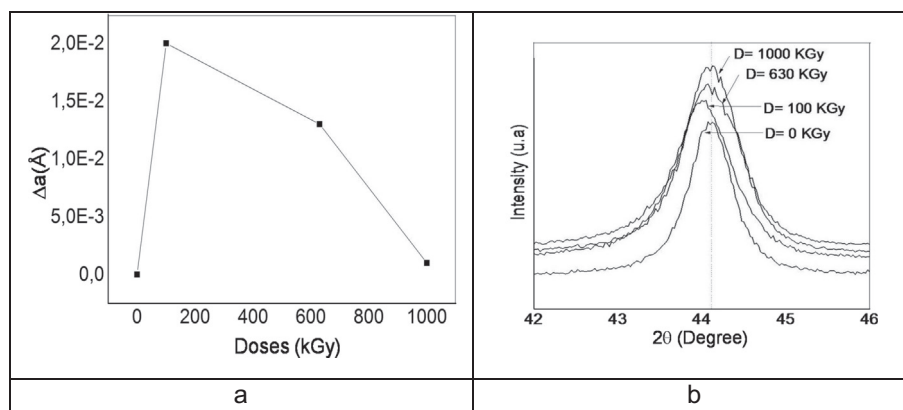


Fig. 5. a) Dependence of the cell parameter in nanometric oxides on the radiation dose. b) Shifts of the (400) XRD maxima at different doses.

Table 2

Atomic positions of non-irradiated LiMn_2O_4 determined by Rietveld analysis at room temperature. Space group $\text{Fd-}3\text{m}$ was used in the analysis. The obtained lattice parameter was $a = 8.205(1) \text{ \AA}$. The R-factors were $R_{\text{exp}} = 13.52\%$, $R_{\text{wp}} = 12.89$, $\text{RB} = 2.12$, $S = 1.44$, and $V = 552.37(9) \text{ \AA}^3$.

Atom	Site	x	y	z	Biso	Occ
Li	8a	1/8	1/8	1/8	1.0	1
Mn	16d	1/2	1/2	1/2	0.81(1)	1
O	32e	0.240(8)	0.240(8)	0.240(8)	1.69(8)	1

Table 3

Atomic positions determined by Rietveld analysis at room temperature of the sample irradiated at 100 kGy. The measurement was performed two years after irradiated. Space group $\text{Fd-}3\text{m}$ was used in the analysis. The obtained lattice parameter was $a = 8.208(2) \text{ \AA}$. The R-factors were $R_{\text{exp}} = 12.89$, $R_{\text{wp}} = 18.7$, $\text{RB} = 2.29$, $S = 1.45$, and $V = 553.02(3) \text{ \AA}^3$.

Atom	Site	X	y	z	Biso	Occ
Li	8a	1/8	1/8	1/8	1.0	1
Mn	16d	1/2	1/2	1/2	0.81(1)	1
O	32e	0.239(3)	0.239(3)	0.239(3)	1.69(8)	1

two phenomena can be observed as a consequence of irradiation.

The first is related to the different decays of the curve near 517 ppm depending on the dose, as shown in Fig. 8 (see the main signal on the left side of the figure). The second phenomenon is related to the deformation of the signal between 560 and 590 ppm in the spectrum (and in the respective side bands) for doses of 630 kGy and 1000 kGy (see side band), as shown in Fig. 8c and d. This is in agreement with the trend observed by XRD of a cell parameter decrease with dose.

The concentration of defects in the nanoparticles and the change in morphology due to relaxation of the defects become significant at a dose of 100 kGy. The way in which these deformations occur is characteristic of anisotropic shielding because of the non-isotropic magnetic distribution around the Li^+ ions [28].

In normal spinel LiMn_2O_4 , each Li^+ ion is surrounded by a symmetric environment of equivalent positions of O^{2-} , Mn^{3+} and Mn^{4+} ions. When the number of shifted Mn ions that form dislocations is high enough in comparison to the size of the nanocrystal, the loss of symmetry around Li^+ is different for each orientation with respect to the external magnetic field.

UV-Vis measurements (Supplementary file) as well as NMR measurements (Fig. 8), shows large variations between the samples irradiated in 630 kGy with respect to the non-irradiated and irradiated at 100 kGy samples, respectively. In this case, it was observed a dramatic rising of a band centered in 5 eV. This band reveals the formation of F centers into the structure due to the oxygen ions shifting.

The DSC study of nanometric LiMn_2O_4 in the temperature range of -30 to 30°C reveals a different behavior than that observed in the micrometric samples. In this material, JT distortion is not observed for the non-irradiated sample or for the samples irradiated at different doses (Fig. 9).

The fact that JT distortion is absent in the non-irradiated nanometric sample can be related to the fact that the crystalline structure of the nanometric material presents structural parameters, such as the Mn–O bonding distance, that exhibit different behaviors with respect to those of the micrometric material. Details will be provided in the next section.

Once the nature of these defects is known, we can propose a model to explain their influence on the JT distortion enthalpy as well as the corresponding benefit to the electrochemical properties, as has been reported for this material [2, 26].

3.2. Action of defects on the JT distortion

Before explaining the effect of defects on the JT distortion, let us depict the situation in which the MnO_6 octahedrons are involved around the main defects (partial and total edge dislocations) in these irradiated samples.

At an edge dislocation, as shown in Fig. 6c, the additional inserted Mn plane generates large repulsions with the neighboring Mn^{3+} , Mn^{4+} and O^{2-} ions forming part of the structure, as shown in Fig. 10. In addition, as shown above, along the dislocation area, the interlayer space grows dramatically. Loss of crystalline orientation and the increased interlayer generate a region that spreads throughout the dislocation, where the cooperative arrangement of JT distortions fades away and consequently the transition vanishes.

At a partial dislocation, the change in symmetry from octahedral to tetrahedral around the Mn^{3+} ions induces the breakage of the Mn–O bond in the c direction, and consequently, the cooperative effect of the JT distortions is mitigated.

As previously noted, a higher degree of crystallinity should allow the cooperative sum of the local deformation produced by the Mn^{3+} octahedrons to overcome the stability of the cubic symmetry [29]. The loss of directionality and increase in the Mn–O distance around dislocations or oxygen defects are the facts of major importance that attempt against JT distortion. Their implications in the micrometric and nanometric oxides are discussed in the following paragraphs.

As shown in Section 3.1.1, the irradiated micrometric oxide presents total edge dislocations running through the [111] direction, and small changes in the plane orientation can be observed in the [111] and [220] directions. Furthermore, a large increase in the interlayer distance can be observed around the dislocation area. Changes in the plane orientation as well as dislocations limit the region in which cooperative distortion take place.

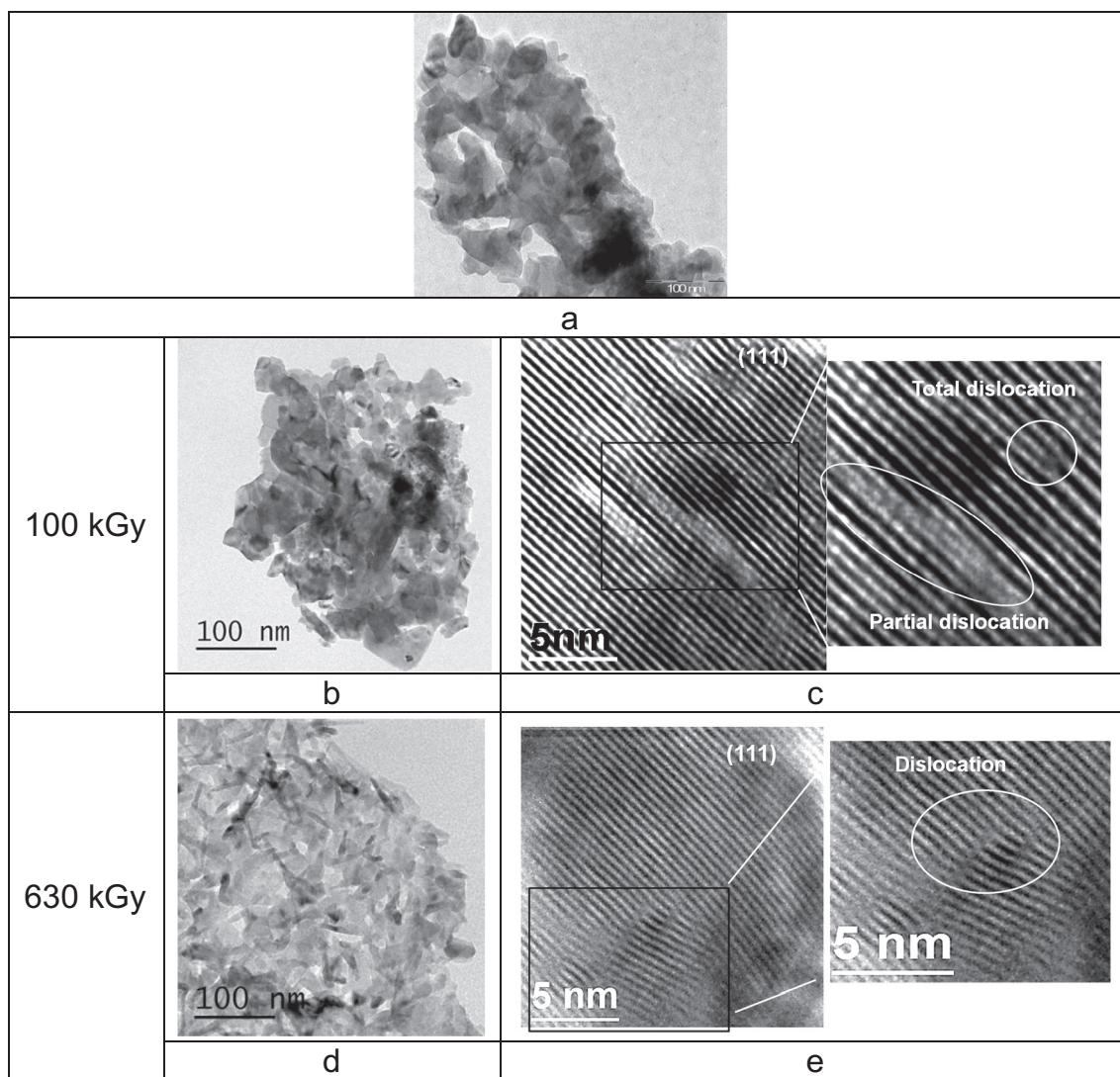


Fig. 6. HRTEM of the irradiated and non-irradiated nanometric oxides: a) non-irradiated oxide, b) oxide irradiated at 100 kGy, c) HRTEM image of the oxide irradiated at 100 kGy, d) oxide irradiated at 630 kGy, e) HRTEM image of the oxide irradiated at 630 kGy.

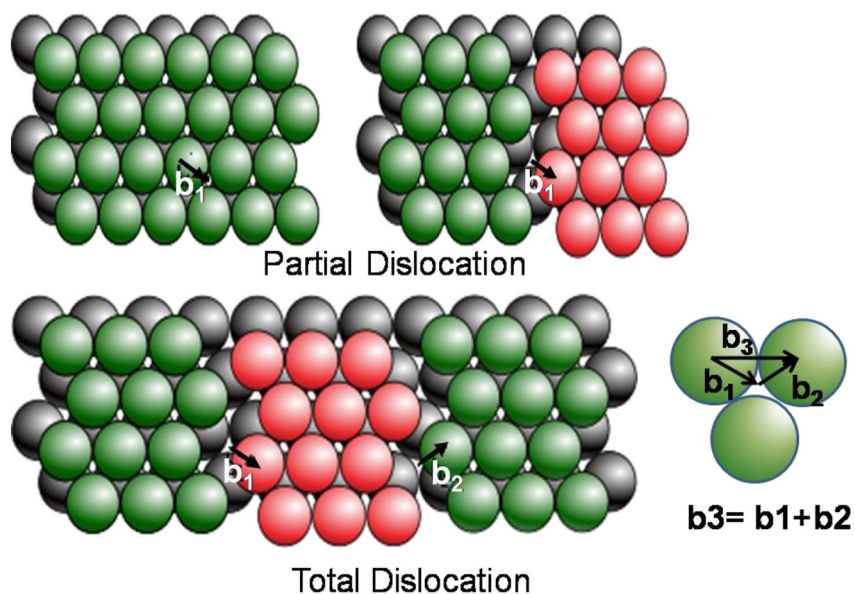


Fig. 7. Vectors (b_1 , b_2 and b_3) describing the formations of partial and total dislocations in the fcc spinel structure.

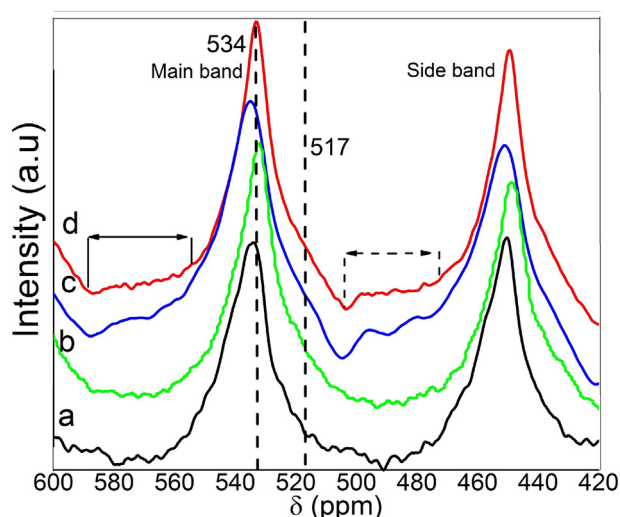


Fig. 8. ^7Li NMR-MAS of the nanometric oxide: a) non-irradiated oxide and b,c,d) oxide irradiated at 100, 630 and 1000 kGy, respectively.

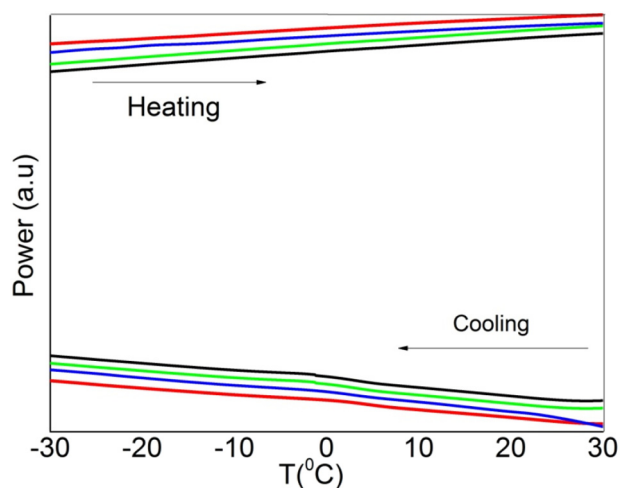


Fig. 9. DSC analysis of the nanometric samples: non-irradiated oxide (black line), oxide irradiated at 100 kGy (green line), oxide irradiated at 630 kGy (blue line), and oxide irradiated at 1000 kGy (red line). (For interpretation of the references to colour in this figure legend, the reader is referred to the web version of this article.)

The effect of the metal-ligand bond distance was rigorously discussed by I.B.Bersuker et al. [30]. In an octahedral system, the JT energy depends quadratically on the metal-ligand bond strength in the direction of the distortion (c), as shown in Fig. 10. The decrease in the JT energy in the micrometric oxide can be explained by the increase in the Mn–O bond length along the dislocation. Additionally, the distortion of the manganese octahedrons along the dislocation contributes to spreading the distortion away from the c direction.

To explain the absence of JT distortion in the non-irradiated and irradiated nanometric oxides, valuable insights can be obtained from the calculations of the average lithium-oxygen ($d_{\text{Li-O}}$) and manganese-oxygen ($d_{\text{Mn-O}}$) bond distances and the average angle formed between oxygen-manganese and the MnO_6 octahedral axis (O–Mn–Axe). Table 4 displays these parameters for the non-irradiated nanometric oxide as well as for previously reported bulk crystalline structures of cubic LiMn_2O_4 (Fd-3 m) and orthorhombic LiMn_2O_4 (Fddd).

Despite the lower value of the cell parameter in the nanometric oxide ($a = 8.205(1) \text{ \AA}$) with respect to that usually found ($a = 8.245 \text{ \AA}$) in a well-crystallized bulk oxide, such as cubic- LiMn_2O_4 (# ICSD 155665), in the nanometric oxide, $d_{\text{Mn-O}}$ is larger than that in the

crystalline cubic structure, as shown in Table 4. As can be observed in the nanometric materials, $d_{\text{Mn-O}}$ suffers a large expansion at the expense of decreasing the Li–O bond distance. In Table 4, a slight difference exists in the O–Mn–Axe angles of these two oxides. This angle is important to measure the average distortion of the MnO_6 octahedrons in the sample for comparison with the ideal structure.

$d_{\text{Mn-O}}$ in the nanometric material is also greater or comparable to the equilibrium bond distances reported for the orthorhombic LiMn_2O_4 phase [31–33] (# ICSD 155 665). Additionally, despite an increase in some of the O–Mn–Axe angles after the cubic to orthorhombic distortion, most of these values remain comparable to that of the nanometric oxide. The fact that $d_{\text{Mn-O}}$ in the nanometric material is larger or comparable to that in the orthorhombic material allows to conclude that in nanometric materials, the forces responsible for driving the JT distortion are already compensated. This gives rise to a lack of energy able to drive the distortion. Furthermore, the small size of the nanocrystal prevents long-range JT cooperative effects and consequently the possibility to carry out the full structural transformation.

Stable defects in the samples irradiated for 2 years give rise to an octahedral array that is more expanded and slightly more distorted, providing similar images as the non-irradiated nanomaterial. Table 5 displays the values obtained for the average lithium-oxygen ($d_{\text{Li-O}}$) bond distance, the manganese-oxygen bond distance in the z direction ($d_{\text{Mn-O}}$) and the angle formed between oxygen-manganese and the z axis (O–Mn– z) of the MnO_6 octahedron. The same parameters are also shown for the bulk tetragonal phase (I41/amd) of $\text{Li}_2\text{Mn}_2\text{O}_4$. The $\text{Li}_2\text{Mn}_2\text{O}_4$ structure is the phase into which LiMn_2O_4 transforms after it is electrochemically lithiated.

In Table 5, it can be observed that the irradiated nanomaterial has a $d_{\text{Mn-O}}$ value (Table 5) even greater than that obtained for the non-irradiated nanometric oxide (Table 4). Consequently, the Li–O bond distance is shorter. Additionally, the O–Mn– z angle exhibits a slightly greater value, which indicates that the MnO_6 octahedrons are slightly more distorted in this direction.

When cubic bulk LiMn_2O_4 transforms into tetragonal $\text{Li}_2\text{Mn}_2\text{O}_4$ oxide in lithium-ion batteries, elongation of the Mn–O bond distance along the z direction occurs. As shown in the nanometric material, when $d_{\text{Mn-O}}$ of both the cubic and the corresponding distorted phase at low temperature (LiMn_2O_4 , Fddd) are similar, the energy driving the distortion vanishes. On the other hand, it was shown that in the irradiated micrometric oxide, an increase in the interlayer distance contributes to reducing the JT distortion energy. All, the similarity between the $d_{\text{Mn-O}}$ of the irradiated nanometric LiMn_2O_4 and tetragonal $\text{Li}_2\text{Mn}_2\text{O}_4$ as well as the presence of oxygen defects and partial and total dislocations in the irradiated nanometric LiMn_2O_4 , support the idea that in this case, JT distortion will barely occur when the defective irradiated material is used in lithium-ion batteries over the 4 to 3 V region.

Finally, the previous results allow us to conclude that dislocations and any defects that induce an increase in the Mn–O distance and the distortion of the MnO_6 octahedron, for instance, oxygen shifting or cavities, can positively influence the mitigation of the JT distortion, thus improving the performance of the material in a battery.

Because the JT effect presents a monotonic growth relationship with the corresponding lattice distortion (c/a) ($\Delta H_{\text{JT}} \sim [c/a-1]$) [29], as long as ΔH_{JT} is diminished the c/a ratio will follow the same tendency [29]. That fact appears to be very advantageous, as it decreases heterogeneous expansion and contraction of the crystalline structure during battery cycling. It has been shown that mechanical stress can lead to the brittle fracture of the material [3, 34]. This happens because physically one single particle is asymmetrically constrained by its neighbor particles generating strain contours, extended defects and micro-cracks [34]. Avoiding the large asymmetrical changes previously observed, it is possible to expand the capacity of the material and to increase the useful life of the battery.

In fact, the previously shown relationship between ΔH_{JT} and the c/a

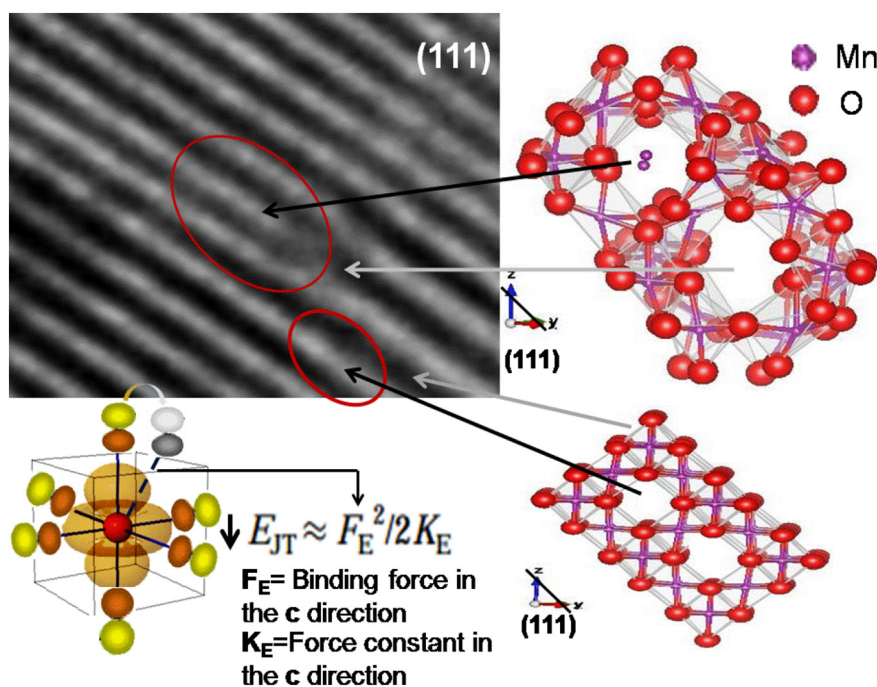


Fig. 10. Influence of the distortion of the manganese octahedrons on the JT distortion energy.

Table 4

Structural parameters of nanometric LiMn_2O_4 , bulk LiMn_2O_4 (Fd-3 m) and orthorhombic LiMn_2O_4 (Fddd). The superscripts indicate the different net positions corresponding to Mn or Li ions.

Composition	dMn-O (Å)	dLi-O (Å)	(O-Mn-Axe) (°)
nano- LiMn_2O_4	2.136(3)	1.645(8)	3.1
cubic- LiMn_2O_4 (# ICSD 155665)	1.9607	1.96934	4.4
orto- LiMn_2O_4 (# ICSD 155665)	2.0186 ¹	1.9762 ¹	6,4
	1.9834 ²	1.9836 ²	4,8
	2.0117 ³	2.0048 ³	5,7
	1.9114 ⁴	1.9416 ⁴	4,6
	1.9151 ⁵		3,9

Table 5

Structural parameters of the obtained irradiated (100 kGy) nanometric LiMn_2O_4 and bulk $\text{Li}_2\text{Mn}_2\text{O}_4$ (I41/amd).

Composition	d ₂ Mn-O (Å)	dLi-O (Å)	(O-Mn-z) (°)
Irradiated nano- LiMn_2O_4 (D = 100 kGy)	2.143(2)	1.625(4)	3.4
$\text{Li}_2\text{Mn}_2\text{O}_4$ (#ICSD 201557)	2.30113	1.8986 ¹	1.8
		2.1491 ²	

ratio as well as the capability of defects to decrease the value of ΔH_{JT} , helps us understand why defects play an important role in the reversibility of defective materials when used in a battery [1, 26, 29, 35]. Defects represent a possible path towards dynamic strength relaxation in materials used in batteries, as is usually reported [24, 26].

However, because of their influence on ΔH_{JT} , they allow the magnitude of the JT structural distortion to be smaller.

4. Conclusions

^{60}Co gamma irradiation of LiMn_2O_4 generates partial and total edge dislocations. Due to the presence of these dislocations, the manganese and lithium ions modify their surroundings and coordination. Furthermore, oxygen shifting can be inferred. These aspects have the greatest influence on nanometric material, from which a large increase

in the cell parameter was observed together with the apparition of the F center band, respectively.

The modification of the Mn surroundings to form dislocations gives rise to the local deformation of its polyhedron. The combined action of the increased Mn–O bond distance in the nanoparticles and the dislocation plane together with the loss of directionality of this bond along the c axis and the formation of oxygen vacancies reduce the phase distortion enthalpy to less than that of a material with perfect polyhedra. This was clearly observed by comparing the DSC measurements of irradiated and non-irradiated micrometric samples.

Because defects lower the ΔH_{JT} of LiMn_2O_4 , a minor distortion of the cell parameter (c/a) should be expected when this material is used as a cathode in lithium-ion batteries. Furthermore, reduced stress between particles should occur; hence, this material should provide better battery performance. This fact has been supported by many papers examining the role that nanoparticles and other defective materials play when passing from the 4 V to the 3 V zone in a reversible manner.

Supplementary data to this article can be found online at <https://doi.org/10.1016/j.ssi.2018.06.007>.

Acknowledgments

This work has been supported by the CAPES-MES # 212/13 and Basic Science Cuban Program (PNCB-18) Projects, as well as the CONACyT-Mexico under grant CB-2015/253342.

References

- [1] Y.M. Masashi Okubo, Hirotochi Yamada, Jedeok Kim, Eiji Hosono, Haoshen Zhou, Tetsuichi Kudo, Itaru Honma, Fast Li-Ion insertion into nanosized LiMn_2O_4 without domain boundaries, *Am. Chem. Soc. Nano* 4 (2010) 741–752.
- [2] Z.L. Hui Xia, Xie Jianping, Nanostructured LiMn_2O_4 and their composites as high-performance cathodes for lithium-ion batteries, *Prog. Nat. Sci.: Mater. Int.* 22 (December 2012) 572–584.
- [3] F.C. Fernanda, R.M.T. Bazito, Cathodes for lithium ion batteries: the benefits of using nanostructured materials, *J. Braz. Chem. Soc.* 17 (2006) 627–642.
- [4] M.T. Hikari Shigemura, Kobayashi Hironori, Sakaebe Hikari, Hirano Atsushi, Kageyama Hiroyuki, Structural and electrochemical properties of $\text{Li}(\text{Fe}, \text{Co})_x\text{Mn}_{2-x}\text{O}_4$ solid solution as 5 V positive electrode materials for Li secondary batteries, *J. Mater. Sci.* 12 (2002) 1882–1891.
- [5] S.L.G. Gurpreet Singh, R.PrasadS. Auluck, Rajeev Gupta, Anjan Sil, Suppression of Jahn–teller distortion by chromium and magnesium doping in spinel LiMn_2O_4 : a

- first-principles study using GGA and GGA + U, *J. Phys. Chem. Solids* 70 (2009) 1200–1206.
- [6] M. Wohlfahrt-Mehrens, Positive Electrode: Manganese Spinel Oxides, (2009).
- [7] C.S. P. Axmann, Positive Electrode: High-Voltage Materials, Elsevier B.V., 2009.
- [8] K. Amine, H. Yasuda, Y. Fuiita, A new three-volt spinel $\text{Li}_{1-x}\text{Mn}_{1.5}\text{Ni}_{0.5}\text{O}_4$ for secondary lithium batteries, *J. Electrochem. Soc.* (1996) 143.
- [9] L. Xiao, Influence of particle sizes and morphologies on the electrochemical performances of spinel LiMn_2O_4 cathode materials, *J. Power Sources* 225 (2013) 286–292.
- [10] H.L. Yonggang Wang, Ping He, Eiji Hosono, Haoshen Zhou, Nano active materials for lithium-ion batteries, *Nano* 2 (2010) 1294–1305.
- [11] R.S. C A Gilbert, S.D. Kenny, S.T. Murphy, R.W. Grimes, a.J.A. Ball, A theoretical study of intrinsic point defects and defect clusters in magnesium aluminate spinel, *J. Phys. Condens. Matter* 21 (2009).
- [12] R.P. Gupta, Radiation-induced cation disorder in the spinel MgAl_2O_4 , *J. Nucl. Mater.* 358 (2006) 35–39.
- [13] S.P. Gokov, S.S. Kochetov, V.I. Kasilov, Yu.G. Kazarinov, Defects Formation in Spinel Crystals Under Electron and Gamma Beam Irradiation (ВОПРОСЫ АТОМНОЙ НАУКИ И ТЕХНИКИ), 93 (2009), pp. 43–45.
- [14] V.T. Gritsyna, I.V.A.-C, Yu.G. Kazarinov, K.E. Sickafus, Optical transitions in magnesium aluminate spinel crystals of different compositions exposed to irradiation, *Nucl. Inst. Methods Phys. Res. B* 218 (2004) 264–270.
- [15] S.J. Zinkle, Radiation-induced effects on microstructure, *Comprehensive Nuclear Materials*, 1 2012, pp. 65–98.
- [16] R. Arabolla Rodríguez, Y.M.L. E. Pérez Cappe, M.A. Aguilar Frutis, J. Santoyo Salazar, O. Luiz Alves, A new strategy toward enhancing the phosphate doping in $\text{Li}_x\text{Mn}_2\text{O}_4$ cathode materials, *Ceram. Int.* 40 (2014) 12413–12422.
- [17] A. Le Bail, D.H.y.F.J.L, Ab-initio structure determination of LiSbWO_6 by X-ray powder diffraction, *Mater. Res. Bull.* 23 (1988) 447–452.
- [18] J. Rodríguez-Carvajal, Fullprof: a program for Rietveld refinement and pattern matching analysis, *Memorias. XV Congress of the IUCr. Satellite meeting on powder diffraction. Toulouse, Francia, 16–19 julio 1990*, p. 127.
- [19] F.W. Young Joo Lee, Sanjeev Mukerjee, James McBreen, Clare P. Greya, ^6Li and ^7Li magic-angle spinning nuclear magnetic resonance and in situ X-ray diffraction studies of the charging and discharging of $\text{Li}_x\text{Mn}_2\text{O}_4$ at 4 V, *J. Electrochem. Soc.* 147 (2000) 803–812.
- [20] V.W.J. Verhoeven, I.M.d.S, G. Nachtegaal, A.P.M. Kentgens, E.M. Kelder, J. Schoonman, F.M. Mulder, Lithium dynamics in LiMn_2O_4 probed directly by two-dimensional ^7Li NMR, *Phys. Rev. Lett.* 86 (2001).
- [21] G.S. White, R.V.J, J.H. Crawford Jr., Optical spectra of MgAl_2O_4 crystals exposed to ionizing radiation, *J. Appl. Phys.* 53 (1981).
- [22] G.P. Summers, Radiation damage in MgAl_2O_4 , *Phys. Rev. B* 21 (1980) 2578–2584.
- [23] L.E. Halliburton, L.A.K, Radiation-induced oxygen interstitials in MgO , *Solid State Commun.* 26 (1977) 111–114.
- [24] C. Kittel, Dislocation, Introduction to Solid State Physics, John Wiley and Sons, Canada, 1996, pp. 585–607.
- [25] R. Hull, C.J, R.M. Osgood, Jr.J. Parisi, Z. Wang, H. Warlimont (Eds.), Dislocation Dynamics During Plastic Deformation ed. 0933-033X, Springer Series in Materials Science Springer Heidelberg, Dordrecht London New York, 2010.
- [26] Y.J. Park, J.G.K, M.K. Kim, H.G. Kim, H.T. Chung, Y. Park, Electrochemical properties of LiMn_2O_4 thin films: suggestion of factors for excellent rechargeability, *J. Power Sources* 87 (2000) 69–77.
- [27] Morsi M. Abou-Sekkina, A.M.K, Fouad G. El-Metwaly, Synthesis, Characterization and Effect of γ -Ray on Rare-Earth Tb^{3+} Doped Nano Lithium Manganates ($\text{LiMn}_2\text{-xTbxO}_4$), 3 (2013).
- [28] M.J. Duer (Ed.), Solid-State NMR Spectroscopy: Principles and Applications, Blackwell Science, 20022001035179.
- [29] M.T. Atsuo Yamada, Koichi Tanaka, Koji Sekai, Jahn–Teller instability in spinel Li–Mn–O , *J. Power Sources* 81–82 (1999) 73–78.
- [30] I.B. Bersuker, Modern aspects of the Jahn – Teller effect. Theory and applications to molecular problems, *Chem. Rev.* 101 (2001) 1067 – 1114.
- [31] K. Kodama, Local lattice distortion caused by short range charge ordering in LiMn_2O_4 , *J. Phys. Soc. Jpn.* 82 (2013) 094601–094607.
- [32] R. Kanno, *Mater. Trans.* 45 (2004) 2048–2055.
- [33] V. Massarotti, LiMn_2O_4 low-temperature phase: synchrotron and neutron diffraction study, *J. Appl. Crystallogr.* (1999) 1186–1189.
- [34] H. Wang, *J. Electrochem. Soc.* 146 (1999) 473–480.
- [35] A.R. Naghash, J.Y.L, Preparation of spinel lithium manganese oxide by aqueous coprecipitation, *J. Power Sources* 85 (2000) 284–293.